LIMNOLOGY
and
OCEANOGRAPHY

ASLO

Limnol. Oceanogr. 9999, 2022, 1–17

doi: 10.1002/lno.12213

Biological influences on coastal muddy sediment structure following resuspension

William Cyrus Clemo,[1,2*] Katelyn D. Giles,[1,2,a] Kelly M. Dorgan[1,2]
[1]Dauphin Island Sea Lab, Dauphin Island, Alabama
[2]School of Marine and Environmental Sciences, University of South Alabama, Mobile, Alabama

Abstract

Shallow coastal muddy sediments are important for global nutrient cycling and carbon storage and provide a habitat for diverse communities of organisms. Bottom shear stress from physical disturbances such as storms and hurricanes resuspend coastal muds, disrupting their cohesive structure. How biological vs. physical processes affect reconsolidation of physically disturbed natural muds, however, is poorly understood. We compare the recovery of sediment properties related to compaction and cohesion of muds following physical disturbance. We hypothesized that recovery of cohesion would take longer than compaction and that changes in surface and subsurface cohesion would occur on different timescales. We collected muddy sediment cores and resuspended the top 5 cm in the lab to simulate storm disturbance. At several timepoints following resuspension (1–30 d), we measured sediment properties providing metrics of compaction (sediment height, porosity, grain size distribution, sound speed) and of surface and subsurface cohesion (erodibility, fracture behavior, exopolymeric substances [EPS]). Compaction and cohesion increased rapidly over the first 1–2 d after resuspension and continued to slowly increase for 2 weeks. Between 2 and 4 weeks, however, subsurface cohesion increased and turbidity decreased, consistent with sediment restabilization. In contrast, subsurface compaction decreased and eroded mass increased, suggesting destabilization. We attribute this apparent destabilization to delayed activity of small-bodied infauna. Surprisingly, EPS concentration did not explain cohesion changes. These results highlight the importance of including biological parameters when predicting the recovery of sediment structure following a physical disturbance. This work has implications for understanding coastal sediment transport dynamics in frequently disturbed sediments.

Shallow, river-influenced coastal muds receive and retain the majority of terrestrial sediment inputs, making them especially important to global nutrient cycling and organic matter processing despite their small areal cover (McKee et al. 2004). Shallow coastal muds are also subject to physical disturbances such as storm-induced wave action that can resuspend sediment, affecting carbon burial and modifying sediment biogeochemical and physical structure (Aller 2004; Wheatcroft et al. 2007; Allison et al. 2010). Because climate change is expected to increase hurricane intensity (Emanuel 2017; Knutson et al. 2020), shallow coastal muds may experience more intense storm disturbances in the future. Understanding how disturbed muds restabilize is also important for coastal engineering applications including riverine sediment diversion, dredge disposal, and channel creation (McAnally et al. 2007; Lo et al. 2014).

In contrast to grain-by-grain erosion that occurs in granular sands, cohesive muddy sediment resuspension occurs through erosion of surface particles, often in the form of loose low-density aggregates, mass failure at planes of weakness below the surface, or bulk fluidization due to excess porewater pressure (Ross and Mehta 1989; Amos et al. 1992; McAnally et al. 2007). Mud erosion is not homogenous but tends to change with sediment depth and shear stress. Most notably, muds have a surface layer of small (100 μm), low-density aggregates that erodes at lower shear stresses than underlying layers (Amos et al. 1992; Thomsen and Gust 2000).

Waves can fluidize muds by creating porewater pressure gradients, leading to pressure buildup that breaks consolidated

---

*Correspondence: wclemo@disl.edu, wclemo@disl.org

Additional Supporting Information may be found in the online version of this article.

[a]Present address: Department of Earth Sciences, University of Memphis, Memphis, Tennessee

Author Contribution Statement: W.C.C. and K.M.D. designed the study. W.C.C. and K.D.G. performed the experiment. W.C.C. analyzed the data with input from other authors. W.C.C. prepared the figures and wrote the 1st draft of the manuscript. All authors contributed revisions, suggestions, and text throughout the manuscript development. All authors read and approved the final submitted manuscript.

sediment into suspended aggregates (McAnally et al. 2007). Lo et al. (2014) showed that although physical consolidation (measured as sediment–water interface height change) of redeposited fluid mud stabilized within 1 week of deposition, erodibility continued to decrease between 2 and 4 weeks after deposition. They suggested this strengthening was due to increasing bonding between sediment aggregates rather than increases in sediment bulk density alone. They did not, however, analyze changes to sediment biological properties other than observing a microbial mat that reduced erosion until it broke up at low shear stresses.

Natural cohesive muds are not simply abiotic clays held together by electrostatic forces but consist of fine mineral grains bound in a sticky organic matrix made up of microbially secreted sediment exopolymeric substances (EPS), which increase sediment cohesiveness (Watling 1988; Decho 2000; Malarkey et al. 2015). Microalgal biofilms comprised of EPS reduce erodibility of surface sediments (Yallop et al. 1994; Widdows et al. 2004; de Brouwer et al. 2005; Lundkvist et al. 2007; Tolhurst et al. 2008). Dickhudt et al. (2009) found no relationship between erodibility and EPS concentration in subtidal estuarine sediments, however, suggesting that microalgal EPS stabilization documented in other studies was not present in light-limited sediments in turbid waters lacking microalgal biofilms. However, Thomsen and Gust (2000) suggested that consolidated muddy sediment beneath a loose aggregate surface layer is less erodible due to microbial EPS. Bulk sediment EPS reduces sand bedload movement and resuspension (Malarkey et al. 2015), but the role subsurface EPS plays in physically disturbed mud reconsolidation has been neglected. Bulk cohesive muds are gel-like solids that fail by fracture (Johnson et al. 2002; Dorgan et al. 2005), and EPS dispersed throughout subsurface sediment may be especially important for post-disturbance redevelopment of this gel-like matrix in subtidal muds in turbid water that lack microalgal biofilms or during periods of low biological activity resulting in reduced EPS production (e.g., winter). EPS stabilization of sediments and sediment stability in general show seasonal variability, generally lower in winter than spring and summer, due to both physical (Dickhudt et al. 2009; Wiberg et al. 2013) and biological (Widdows et al. 2004) factors.

Most marine muds provide habitat for infauna which can act as ecosystem engineers by changing the physical properties of their sediment habitat. Burrowing by infauna can destabilize sediments by loosening compacted sediment (Eagle 1973), disrupting biofilms (Widdows et al. 2000), and resuspending mud (Volkenborn et al. 2007; Soissons et al. 2019). Infauna may also stabilize sediments through tube-building (Eagle 1973; Eckman et al. 1981; Thrush et al. 1996), compacting loosened sediment (Montserrat et al. 2008), stimulating EPS production (Passarelli et al. 2012), or biodeposition (Soissons et al. 2019). Physical disturbance to the sediment can resuspend or smother infauna (Eagle 1973; Brenchley 1981; Thrush et al. 2003), but how physical disturbance and burrowing activity of surviving infauna affect short and long-term sediment stability is less clear, especially in disrupted cohesive muds.

This study examines how different geological and geotechnical properties of natural cohesive muds change over time following physical disturbance to better understand how biological vs. physical processes affect mud restrengthening. We hypothesized that, following physical disturbance, sediment compaction would occur faster than cohesion, which would depend on both increasing density and slower biological processes. We compare the time scales of recovery of surface and subsurface cohesion, hypothesizing that either (1) surface and subsurface cohesion would increase over time at similar rates due to both processes depending on microbial EPS production (sediments were kept in the dark, so bacterial activity was expected to dominate EPS production rather than microalgae); (2) surface cohesion would stabilize more quickly than subsurface cohesion because microbial EPS production would be enhanced by oxic conditions; or (3) subsurface cohesion would stabilize more quickly than surface cohesion because greater overlying sediment weight would compact sediments more quickly and increase contacts among grains. Because we sampled during midwinter in an area where we had previously found low infaunal abundance and sediments were disturbed with no opportunity for recolonization, we expected infauna to be present in low abundances and have negligible effects on sediment properties compared to disturbance effects.

Materials

Overview

We resuspended natural muddy sediment cores and compared changes in sediment compaction to changes in surface and subsurface cohesion over 30 d. We measured sediment–water interface (SWI) height, acoustic sound speed, sediment porosity, and grain size as metrics of physical compaction. Our metrics of cohesion were erodibility, subsurface tensile strength, and sediment EPS, which was predicted to correlate with cohesive strength.

Core collection

We collected cohesive muddy sediment cores from 10 m depth in the northern Gulf of Mexico offshore of Dauphin Island, Alabama, on 26 January 2020 (3013.333^{0}N, 888.348^{0}W). Bottom water at the site was 16.2C and 35 psu. Thirty-five polycarbonate sediment cores (9.6 cm inner diameter 60 cm height) were collected using an Ocean Instruments MC-400 multicorer. The SWI height was marked on the outside of each core. After transport to the Dauphin Island Sea Lab, the SWI heights of the cores had not noticeably changed, indicating negligible compaction. Cores were stored at room temperature in the dark to prevent photosynthesis and under aeration to maintain oxygenated water. Airstones were positioned high enough off the sediment surface to prevent resuspension. Initially, four replicate cores (labeled A through D) were designated for each of the seven sampling timepoints (undisturbed, or Day 0, and 1, 2, 3, 7, 14, and 30 d following resuspension). The remaining cores served as substitute replicates. A 5th replicate (E) was added to Day 2, 3, and 14 timepoints, but there were insufficient cores available to sample 5 cores at every timepoint.

Core resuspension

Two days after collection, we resuspended the top 5 cm of each core (apart from undisturbed cores) with a modified baster. Holes in the baster directed water jets laterally just below the sediment surface and at 5 cm depth (Fig. 1a). We squeezed the baster three times, rotated it 90, and squeezed three more times. We repeated the series of six baster squeezes three times every hour for 12 h. The resuspension depth, 5 cm, is approximately half the global average biologically mixed sediment layer, and disturbance of this layer would likely impact infaunal habitat suitability (Boudreau 1998). This depth is also within range of major hurricane sediment mixing depth in shallow (< 20 m) water (Morton 1988; Bentley et al. 2002). The resuspension duration, 12 h, is consistent with timescales of hurricane passage over coastal waters (Morton 1988, Bentley et al. 2002). We sampled 4–5 replicate cores for sediment properties 1, 2, 3, 7, 14, and 30 d following resuspension. Thirty days were chosen based on observations by Lo et al. (2014) that erodibility of redeposited mud took at least 4 weeks to reach values similar to those of nearby natural undisturbed mud. Thirty days are also within range of time between storms likely to cause sediment resuspension at our collection site. Due to complications with the erosion chamber and acoustics equipment at the beginning of the experiment, we lost several undisturbed Day 0 cores, which resulted in too few replicates to include.

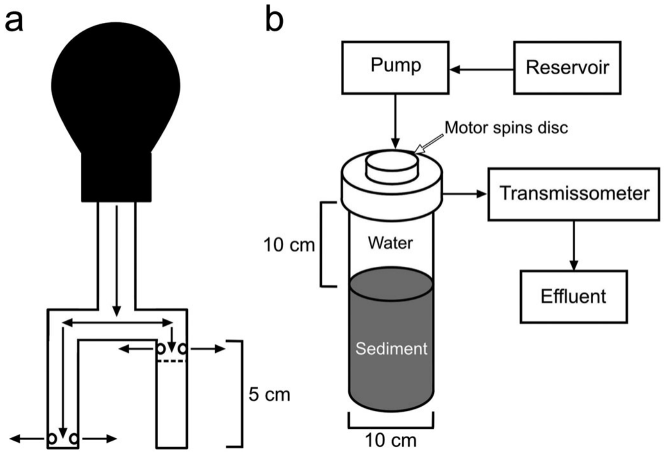

Fig. 1. (a) Diagram of modified baster used to resuspend sediment and (b) diagram of Gust erosion chamber. Black arrows indicate water flow direction. Diagrams not drawn to scale.

Sediment compaction

To quantify short- and long-term sediment compaction continuously and nondestructively, we measured post-disturbance SWI height above the core base 16 times over 30 d following disturbance. For each core, the predisturbance SWI height was subtracted from the SWI heights at each timepoint to provide SWI height above or below the undisturbed height. SWI heights higher than the undisturbed height indicated less compact sediment.

Sound speed through sediment was measured over the 30 d to capture temporal change through a nondestructive measurement of sediment compaction. For the sandy muds in this study, increasing sediment bulk density (i.e., increasing compaction) results in faster sound speed (see fig. 5.2 in Jackson and Richardson 2007). We performed acoustic measurements following methods from Dorgan et al. (2020). Within a seawater tank, a 400-kHz three-cycle sinusoidal tone burst was transmitted horizontally through sediment cores to a receiver at three depths below the sediment surface (2.5, 5, and 10 cm) (see fig. 1 in Dorgan et al. 2020). To account for sound speed differences due to temporal variability in temperature and salinity, sound speed through sediment was normalized by the sound speed in seawater to obtain sound speed ratio (SSR). Sound speed in seawater (c_w) and the time of flight through sediment (t_s) and seawater cores (t_w) (calculated as lag time between the transmitted and received signals) were used to calculate sound speed in sediment (v_p):

$$v_p = \frac{c_w}{1 - c_w \frac{(t_w - t_s)}{d_s}} \qquad (1)$$

where d_s is the inner diameter of the core (Jackson and Richardson 2007; Dorgan et al. 2020). SSR was then calculated by dividing v_p by c_w, where a higher SSR indicates more compact sediment. SSR measurements were also performed on cores destructively sampled 30 d after resuspension (Day 30 C) at timepoints prior to the end of the experiment to examine temporal changes within the same set of cores.

We subsampled cores with a 2.3-cm-diameter syringe core to a depth of 10 cm and sectioned in 1 cm increments to examine changes in porosity and grain size within and below the disturbed layer. We subsampled these 1 cm sections for EPS measurement, and all sediment was frozen at 80C. We calculated water content from sediment mass differences before and after drying at 65C for 24 h as mass of water divided by mass of dry sediment (eq. 4.7 from Jackson and Richardson 2007). Porosity (β) was then calculated from water content (w):

$$\beta = \frac{w}{\frac{\rho_w}{\rho_g} + w} \qquad (2)$$

where ρ_w is seawater density, and ρ_g is sediment particle density (table 4.5 from Jackson and Richardson 2007). A ρ_w of

1025 kg m^3 was calculated using the equation of state for seawater (Jackson and Richardson 2007) based on an average temperature of 20C and salinity of 35 psu, and a ρ_g of 2650 kg m^3 was used assuming quartz as the dominant mineral composing sediment particles in this study (table 4.7 from Jackson and Richardson 2007). Assuming a density of quartz neglects the effects of solid organic matter on overall sediment density and may overestimate porosity (Avnimelech et al. 2001). However, because we collected our sediment from the same location, we did not expect differences in porosity to be strongly affected by the exclusion of organic content from porosity calculations. We measured grain size every cm in the top 5 cm and at 8 and 10 cm for undisturbed cores and cores 3 and 30 d after resuspension. We determined grain size distribution with a Malvern Mastersizer 3000 particle analyzer. Data were analyzed with Gradistat (Kenneth Pye Associates, Ltd.) and classified according to Folk and Ward (1957).

Sediment cohesion

To examine changes in sediment surface cohesion, we measured total eroded mass and turbidity using a custom-built Gust erosion chamber (Fig. 1b, Gust and Muller 1997, Thomsen and Gust 2000, Green Eyes, LLC 2015). Cores were capped with the erosion chamber cap in which a rotating disc generated increasing levels of shear stress (0.1, 0.2, 0.3, 0.45, and 0.6 Pa). Each stress level was maintained for 20 min before increasing to the next level. At each stress level, water and eroded material were removed by a pump at the center of the disc 10 cm above the sediment surface. This effluent passed through a Sea-Bird C-Star transmissometer recording light attenuation coefficient (m^1) at 650 nm to determine turbidity over time and was then captured for later filtration. An initial 0.01 Pa interval was used as a flushing step and not filtered, but seawater used to replace the effluent was filtered to determine background suspended sediment concentration (SSC).

Total eroded mass at each stress level was obtained by filtering the effluent through 47-mm Whatman GF/F filters (1.5 μm pore size). Filters were dried at 65C for 24 h, then weighed. We calculated SSC, C_s (kg m^3), for each core at each stress level from the dry mass (kg) of filtered sediment divided by the volume (m^3) of water filtered. C_s was converted to eroded mass per area (E; kg m^2):

$$E = \frac{C_s V_c}{A_c}, \tag{3}$$

where V_c is chamber volume (7.24 10^4 m^3), and A_c is sediment surface area (7.24 10^3 m^2). To generate specific shear stresses, we set cap rotation and pumping rate using established calibration equations (Green Eyes, LLC 2015):

$$u_{15} = 0.0318 n^{0.763}, \tag{4}$$

$$Q = 28.31 u_{15}^2 + 170.2 u_{15}\ 23.85, \tag{5}$$

where u_{15} is shear velocity at 15C (cm s^1), n is rotations per minute, and Q is pumping rate (mL min^1). Shear velocity at 15C was converted to shear velocity at the average water temperature measured during the erosion tests (20C) as:

$$u_{15} = u_{20}[1 + 0.006(20\ 15)], \tag{6}$$

where u_{20} is shear velocity at 20C (cm s^1) (Green Eyes, LLC 2015). Shear stress (τ_b; Pa) was calculated from shear velocity (u_{20}; m s^1) and seawater density (ρ_w; kg m^3) as (Green Eyes, LLC 2015):

$$\tau_b = \rho_w u_{20}^2. \tag{7}$$

We determined turbidity, as SSC (kg m^3), from light attenuation coefficient, measured continuously throughout each stress level. We calibrated the transmissometer with muddy seawater of four levels of SSC (0.0038, 0.018, 0.030, and 0.050 kg m^3) made from sediment from the coring site. We then filtered each muddy water sample following the steps above to determine SSC and determined the relationship of light attenuation coefficient (c; m^1) and SSC (C_s; kg m^3):

$$C_s = 0.17c + 0.0015. \tag{8}$$

To determine subsurface cohesion changes over time, we measured tensile force (N) using a custom probe modified from a fracture toughness probe developed by Johnson et al. (2012). A helical probe is rotated and translated into the sediment like a corkscrew, then pulled upward, breaking off a plug of sediment. Force, measured with an in-line force sensor (Futek LS-200 2-lb), increases to a peak force, then drops when the plug breaks free of the sediment below. Forces from friction with the surrounding sediment and the weight of the sediment plug are removed by repeating the corkscrew motion and subtracting the force profile from the 2nd upward pull. The peak force in the plot of net force as a function of upward distance corresponds to the tensile strength of the sediment, a metric of cohesion. These force measurements are comparable across the same depth in different cores, with higher force indicating greater cohesion.

To determine if differences in erodibility and tensile strength were driven by variability in surface and subsurface EPS, we analyzed the subcore for EPS carbohydrate concentrations. We differentiated between water-soluble (colloidal) and sediment-bound EPS as we expected bound EPS to contribute more to cohesion because they are directly bound to sediment grains rather than dissolved in porewater. Following methods of de Brouwer and Stal (2001), we lyophilized frozen sediment and extracted colloidal carbohydrates with purified water for 1 h at 30C. We then extracted bound carbohydrates with

0.1 M Na_2EDTA for 16 h at room temperature. We measured both carbohydrate fractions with the sulfuric acid-UV assay (Albalasmeh et al. 2013), which is based on the phenol-sulfuric acid assay (Dubois et al. 1956). An amount of 900 µL 96% sulfuric acid was added to 300 µL carbohydrate solution to dehydrate dissolved carbohydrates into furfural derivatives, which absorb UV light. This solution was vortexed for 30 s, allowed to return to room temperature for approximately 5 min, then UV absorbance at 315 nm was measured using a SpectraMax M5 microplate reader. We determined carbohydrate concentration from UV absorbance of a glucose reference.

Because we expected changes in sediment compaction and cohesion to stabilize over time at different time points, we analyzed changes in variables over time by fitting the data to an asymptotic equation of the form:

Y ¼ a ða bÞe^{cX} ð9Þ

where Y is a given measurement, X is time in days, a is the asymptote of Y, b is the Y intercept, and c is proportional to the relative rate of change in Y as X changes. To compare stabilization rates of different variables, the Y value at which a given variable was close to stabilizing over time (Y_{stab}; that is, reaching close to the asymptote) was defined as:

Y_{stab} ¼ a þ 0:05jb aj: ð10Þ

We then calculated the time (X) at which Y_{stab} was reached using Eq. 9. This time is directly proportional to c, allowing comparison of variables with different ranges.

Variables that did not exhibit expected asymptotic trends were analyzed using linear regression. For non-normally distributed variables and variables that exhibited nonlinear but non-asymptotic trends, we treated time points as groups and applied Kruskal–Wallis tests to assess differences among time points. Following significant Kruskal–Wallis tests, we assessed differences between individual time points with a post hoc Dunn–Šidak multiple comparisons test which includes p value adjustment to lower the familywise error rate (Sokal and Rohlf 2012). We assessed normality using the Shapiro–Wilk normality test. We performed all statistical analyses in Matlab (Mathworks).

Because sediment was removed during subcoring and the remaining core was heavily disturbed by the erosion and subsurface cohesion measurements, infauna were not quantitatively sampled. When infaunal activity appeared on the surface, some cores were sieved (500 µm mesh size) for qualitative assessment of the infaunal families that were abundant in cores.

Results

Sediment compaction

Following resuspension, average SWI height decreased rapidly in the first 1–2 d then stabilized close to the original SWI height at 0.118 (0.093–0.329, 95% CI) cm 1.42 d after resuspension (pseudo-R^2 = 0.78, df = 61) (Fig. 2). Sediment porosity ranged from 0.50 to 0.68 within the disturbed layer (2–5 cm) and was highly variable 1 d after resuspension (Fig. 3). There were no significant differences among time points between 2 and 30 d post disturbance at 3 or 5 cm ($p > 0.152$, df = 4) (Fig. 3). We excluded Day 1 from analysis because compaction of fluidized sediment during subcoring prevented accurate measurement of porosity.

Sediment grain size did not change substantially after resuspension. Sediments at all depths and timepoints were generally poorly sorted or very poorly sorted muds or sandy muds and were coarser at depth compared to near the surface (Table 1; Supporting Information Fig. S1). Sediment mean grain size within the disturbed layer was within the medium silt range and became coarser below the disturbed layer, with neither layer changing significantly over time (Table 1, $p > 0.379$, df = 2). Mud fraction, consisting mostly of silt, was higher than sand fraction and was similarly higher in the disturbed layer than at depth, but no sediment size fraction exhibited significant temporal differences at either depth (Table 1; Supporting Information Fig. S1, $p > 0.267$, df = 2).

SSR within the disturbed layer (2.5 and 5 cm depths) varied considerably among cores 1 d after resuspension then appeared to slightly increase between Days 3 and 14 then slightly decrease between Days 14 and 30 (Fig. 4a,b, black boxes). SSR among time points differed significantly at 2.5 cm (Kruskal–Wallis χ^2_3 = 13.500, p = 0.004) and 5 cm (Kruskal–Wallis χ^2_3 = 14.054, p = 0.003), but only SSR at Day 14 was significantly greater than on Day 30 at 2.5 cm (adjusted p = 0.004, df = 1) while Day 14 SSR was significantly greater than SSR at both Days 3 and 30 at 5 cm (Day 14 vs. Day 3: adjusted p = 0.023, df = 1; Day 14 vs. Day 30: adjusted

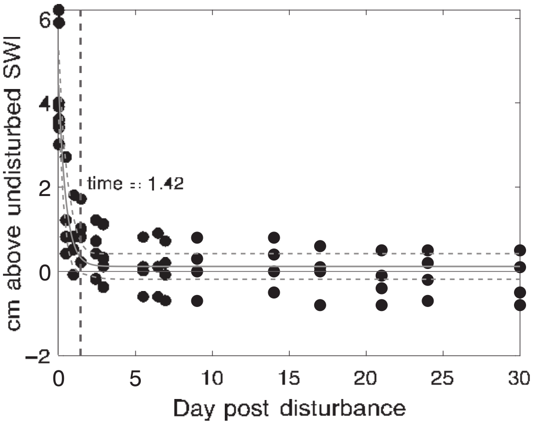

Fig. 2. Distance (cm) above undisturbed SWI height vs. time post disturbance of Day 30 C. Solid and dashed lines indicate asymptotic fit and 95% CI, respectively, of the form Z(t) = 0.118 (0.118 4.425) * $e^{2.117*t}$, where Z is distance above undisturbed SWI (cm) and t is day post disturbance. Vertical dotted line indicates time at which distance above undisturbed SWI stabilizes close to the asymptote.

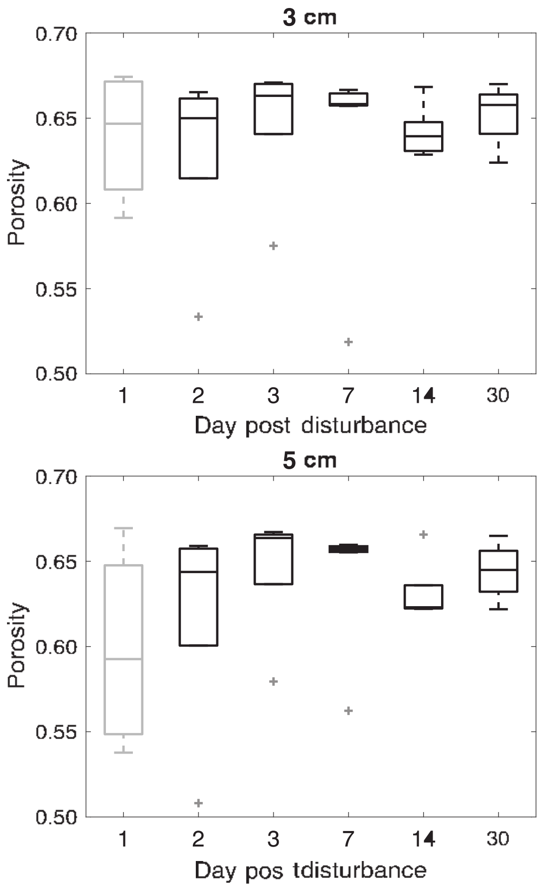

Fig. 3. Sediment porosity at 3 and 5 cm depth for each time point (n = 4–5). Day 1 box plot is gray to indicate it was excluded from Kruskal–Wallis analysis. Median is indicated by center line, box indicates interquartile range of the data, and top and bottom whiskers indicate maximum and minimum values, respectively. Crosses indicate outliers excluded from analysis. “ns” indicates no significant differences among timepoints.

p = 0.004, df = 1). SSR below the disturbed layer (10 cm) was generally more variable, and time points did not differ significantly (Kruskal–Wallis χ^2_3 = 4.868, p = 0.182) (Fig. 4c, black boxes). Due to interference in our acoustic signal on Day 2, we excluded SSR for all Day 2 cores.

Repeated SSR measurements on the cores that were destructively sampled on Day 30 (Fig. 4a–c, gray boxes) performed at the respective time points of the other cores (Fig. 4a–c, black boxes) were similar to SSR of the time point cores within the disturbed layer. The exception was that SSR of Day 1 cores appeared to be more variable than SSR of Day 30 C scanned on Day 1, likely because we scanned Day 30 C later in the day than the Day 1 cores. Within the disturbed layer, SSR differed significantly among time points (2.5 cm: Kruskal–Wallis χ^2_7 = 23.885, p = 0.001; 5 cm: Kruskal–Wallis χ^2_7 = 18.203, p = 0.011), but only SSR on Day 14 was significantly greater than on Days 24 and 30 at 2.5 cm (Day 14 vs. Day 24: adjusted p = 0.016, df = 1; Day 14 vs. Day 30: adjusted p = 0.002, df = 1) and Day 30 at 5 cm (adjusted p = 0.005, df = 1) (Fig. 4a,b, gray boxes). Similar to the individual time point cores, Day 30 core SSR did not differ significantly among time points at 10 cm (Kruskal–Wallis χ^2_7 = 11.647, p = 0.113) (Fig. 4c, gray boxes). These small changes in SSR and porosity within the disturbed layer (2–5 cm) from Days 3 to 30 are consistent with established relationships between SSR and porosity of natural sediments (Buckingham 2005) (Fig. 4d). SSR appeared to increase from Days 3 to 14 as porosity decreased, then SSR decreased while porosity increased between Days 14 and 30 (Fig. 4d).

Sediment cohesion

Turbidity exceeded the transmissometer threshold at several shear stress levels for most timepoints, but the proportion of time in which the threshold was exceeded declined over time post disturbance (Fig. 5a). At lower shear stress levels (0.1 and 0.3 Pa), turbidity remained below the threshold, and peak SSC declined exponentially over time to an asymptote (Fig. 5b,d). At 0.1 Pa, max SSC declined to an asymptote of 0.0105 (0.0059–0.015 95% CI) kg m^3, stabilizing by 4.5 d after disturbance (pseudo-R^2 = 0.71, df = 20) (Fig. 5b). In contrast, max SSC at 0.3 Pa reached an asymptote of 0.0158 (0.0002–0.0313 95% CI) kg m^3, not stabilizing until 25.2 d after resuspension (pseudo-R^2 = 0.60, df = 20) (Fig. 5d). For

Table 1. Average sediment mean grain size and sand, silt, clay, and mud (silt + clay) fractions for undisturbed (Day 0) and 3 and 30 d after resuspension from depths within (1–2 cm) and below (7–8 cm) the disturbed layer. Numbers in parentheses are standard devia-tions. There were no significant differences in grain size characteristics at either depth among timepoints (Kruskal–Wallis test p > 0.267, df = 2).

Time	Depth (cm)	Mean grain size (µm)	Sand fraction	Silt fraction	Clay fraction	Mud fraction
Day 0	1–2	18.8 (5.88)	0.18 (0.11)	0.74 (0.10)	0.08 (0.01)	0.82 (0.11)
(n = 3)	7–8	41.3 (11.0)	0.45 (0.10)	0.52 (0.09)	0.04 (0.01)	0.55 (0.10)
Day 3	1–2	21.6 (13.1)	0.19 (0.17)	0.73 (0.14)	0.08 (0.03)	0.81 (0.17)
(n = 5)	7–8	29.2 (10.1)	0.32 (0.11)	0.62 (0.09)	0.07 (0.02)	0.68 (0.11)
Day 30	1–2	18.7 (5.11)	0.16 (0.08)	0.77 (0.07)	0.08 (0.02)	0.84 (0.08)
(n = 4)	7–8	40.8 (25.5)	0.42 (0.25)	0.52 (0.20)	0.06 (0.05)	0.58 (0.25)

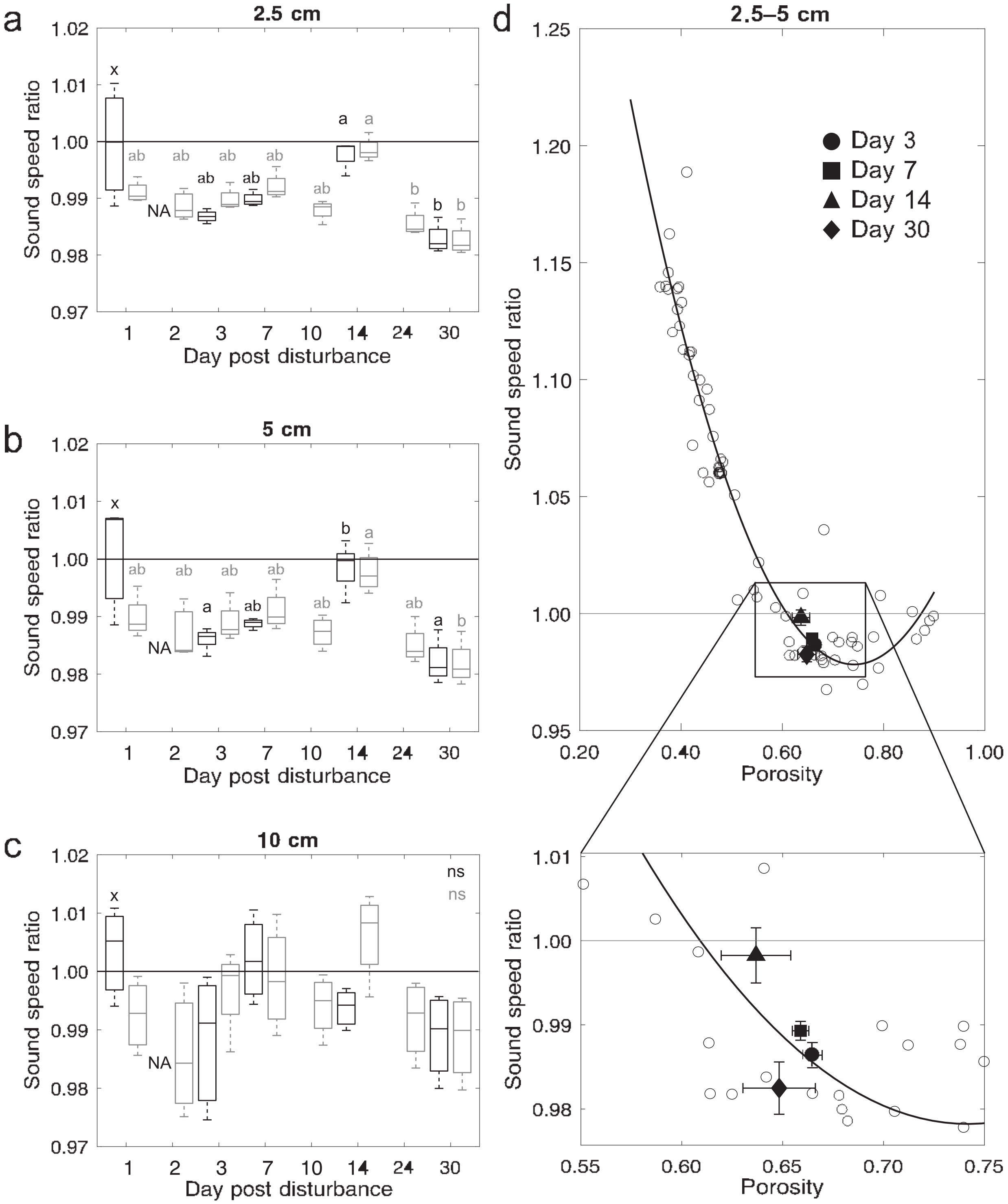

Fig. 4. SSR vs. time post disturbance at 2.5, 5 and 10 cm depths (a–c) and as a function of porosity compared to data from a range of natural sediments (d). SSR for each time point (black boxes; n = 3–5) are plotted with SSR of Day 30 C scanned at several time points (gray boxes; n = 3–4) (a–c). "X" indicates Day 1 SSR excluded from analysis, "NA" indicates excluded Day 2 SSR data, letters indicate Dunn–Šidak comparison differences between time points (black) and Day 30 C scanned at different times (gray), and "ns" indicates no significant differences among timepoints (a–c). Average SSR vs. porosity of the disturbed layer (2.5 and 5 cm) for each time point (filled symbols; n = 3–5) are plotted with data taken from Dorgan et al. (2020) and Buckingham (2005) (open circles), with zoomed-in inset (d). The solid line is a quadratic fit to the Buckingham (2005) data of the form $SSR(\beta) = 1.2379 * \beta^2 - 1.8364 * \beta + 1.6593$, where β is porosity (d). Bars are 1 standard deviation.

the other shear stress levels, max SSC could not be determined due to turbidity exceeding the transmissometer threshold, so we examined the proportion of time above this threshold instead, and times to reach an asymptote are not comparable to those of 0.1 and 0.3 Pa levels. At 0.2 Pa, proportion of time above the turbidity threshold decreased to an asymptote of 0, stabilizing 9.4 d after resuspension (pseudo-R^2 = 0.56, df = 21) (Fig. 5c). Proportion of time decreased more rapidly to 0 at 0.45 Pa (6.8 d; pseudo-R^2 = 0.65, df = 21) (Fig. 5e), but more slowly at 0.6 Pa (36.9 d; pseudo-R^2 = 0.79, df = 21) (Fig. 5f).

Cumulative eroded mass appeared to drop rapidly 1 d after disturbance, then increase again between 2 and 4 weeks, but these patterns varied with shear stress (Fig. 6a). Eroded mass at 0.1 Pa was low and appeared to decline between Days 7 and 30 while eroded mass at 0.2 Pa significantly declined by 9.73 10^5 (4.07 10^5 to 1.54 10^4 95% CI) kg m^2 d^1 (R^2 = 0.35, p = 0.002, df = 20) (Fig. 6b,c). At 0.3 Pa, eroded mass appeared to decline from 1 d to 2 weeks post disturbance and then increase between 2 and 4 weeks (Fig. 6d). Most of the erosion occurred at 0.45 and 0.6 Pa, in which cumulative eroded mass appeared to follow an asymptotic trend until between 14 and 30 d after disturbance (Fig. 6e,f). Eroded mass at 0.45 and 0.6 Pa rapidly declined over time to asymptotes of 0.0182 (0.0158–0.0207 95% CI) and 0.0382 (0.0297–0.0467 95% CI) kg m^2, stabilizing by 0.4 and 1.1 ds after resuspension (pseudo-R^2 = 0.55 and 0.62, df = 15) (Fig. 6e), respectively. However, eroded mass from Days 14 to 30 did not remain stable but appeared to increase (Fig. 6a,d–f).

Observations of erosion behavior showed differences over time that potentially explain the different patterns between turbidity and eroded mass. At earlier time points, eroded sediments were generally in the form of smaller and loosely aggregated particles that created visibly murky water (Fig. 7a,b; Supporting Information Video S1), and scoured furrows often appeared at higher shear stresses (Fig. 6b). By Day 30, however, much of the eroded mass was in the form of large and compact fecal pellets produced by capitellid and spionid annelids. This resulted in relatively high eroded mass but less murkiness (Fig. 6c; Supporting Information Video S1). Scoured furrows did not form during any shear stress level for Day 30 C.

Sediment maximum tensile force was examined at 3, 4, and 7 cm depths, within and below the disturbed layer. Sediment within the disturbed layer 1 d after disturbance was likely still fluid, so tensile force measurements at this time point were likely not reliable and are excluded from analysis. Tensile force measurements from the Day 2 D and Day 3 C cores were also excluded at 3 and 4 cm as they had much lower porosities and higher max tensile force than the other replicates at those time points. The Day 3 C core was also sandier than the other Day 3 cores (Supporting Information Fig. S1). Max tensile force at 3 cm increased over time until reaching an asymptote of 0.129 (0.108–0.150, 95% CI) N, stabilizing by 20.7 d after disturbance (pseudo-R^2 = 0.60, df = 16) (Fig. 8a). Max tensile force at 4 and 7 cm did not appear to reach an asymptote. At 4 cm, max tensile force increased over time at a rate of 0.0049 (0.0029–0.0069, 95% CI) N per day (R^2 = 0.60, p = 6.50 10^5, df = 26) (Fig. 8c). Force at 7 cm was higher and more variable than force at 3 and 4 cm but did not significantly differ among time points (Kruskal–Wallis χ^2_5 = 5.807, p = 0.326). (Fig. 8e). Max tensile force was not correlated with mean grain size, mud, or clay fractions at any depth (Spearman rank correlation; $p > 0.066$, df = 10) but was negatively correlated with porosity at all three depths, consistent with tensile strength increasing with compaction (3 cm: Spearman's ρ = 0.69, p = 0.002, df = 16; Fig. 8b; 4 cm: Spearman's ρ = 0.67, p = 0.002, df = 16; Fig. 8d; 7 cm: Spearman's ρ = 0.52, p = 0.010, df = 16; Fig. 8f).

We examined EPS carbohydrate concentrations in the top 1 cm to compare to erosion measurements and at 3, 4, and 7 cm to compare to max tensile force measurements. Overall, more EPS was sediment-bound than colloidal, but concentrations of both EPS fractions were highly variable and did not significantly differ among time points at any depth (Kruskal–Wallis $p > 0.118$, df = 5), apart from colloidal EPS concentration at 1 cm, which exhibited slightly significant differences among time points (Kruskal–Wallis χ^2_5 = 11.356, p = 0.045). Although there was a trend of increasing colloidal EPS in surface sediments over the first few days, pairwise differences in EPS concentration among individual time points did not differ significantly (adjusted $p > 0.112$, df = 1) (Fig. 9). Neither bound nor colloidal EPS concentrations at 1 cm were correlated with cumulative eroded mass ($p > 0.421$, df = 18), and EPS concentration was not correlated with max tensile force at 3 or 4 cm ($p > 0.175$, df = 16) (Supporting Information Fig. S2). Max tensile force at 7 cm decreased slightly with increasing bound EPS concentration (R^2 = 0.22, p = 0.016, df = 21; Supporting Information Fig. S2), in contrast to our hypothesis that EPS would increase cohesion. Max tensile force at 7 cm was not significantly correlated with water-soluble EPS (p = 0.303, df = 21) (Supporting Information Fig. S2).

Discussion

Delayed infaunal effects on post-disturbance surface cohesion

Most studies documenting infaunal effects on sediment properties generally focus on large and mobile (e.g., burrowing shrimp, large bivalves; Wynberg and Branch 1994, Soissons et al. 2019) or large and highly abundant (e.g., lugworms, *Lanice conchilega* matts; Volkenborn et al. 2007, Rabaut et al. 2007) animals that mix sediments or create rigid structures. The tube-building capitellid and spionid annelids present in this study are much smaller (< 1 mm diameter) and are more often classified by their "pioneering" ability to quickly recolonize and oxidize highly reduced sediments than their sediment mixing behavior (although capitellids can transport sediment from depth to the surface, i.e., "upward conveyor belt feeders") (Fig. 7e, Pearson and Rosenberg 1978, Queiros et al. 2013, Jumars et al. 2015). Because we expected negligible infaunal abundance and therefore effects on disturbed sediment properties

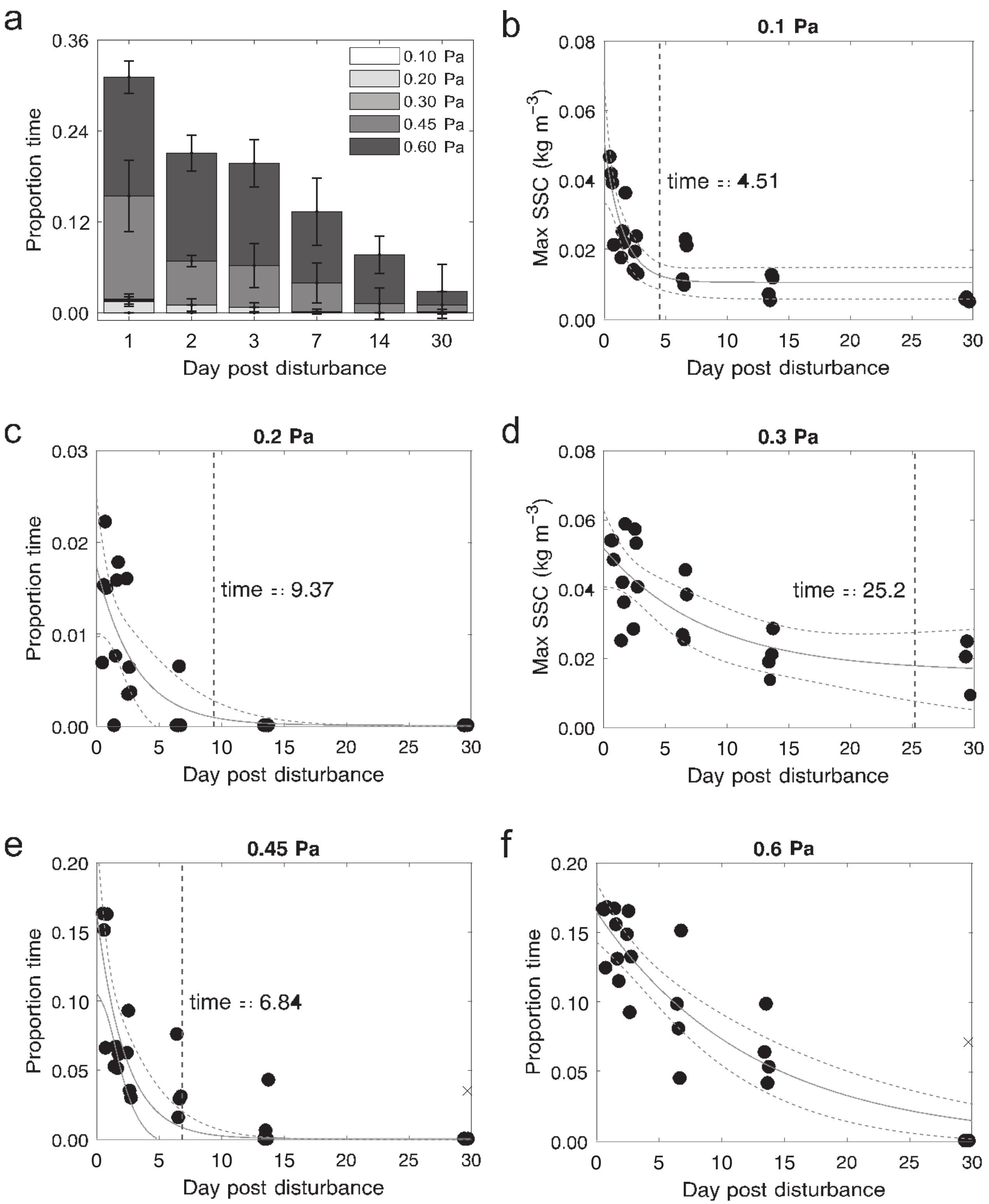

(Figure legend continues on next page.)

and initially observed little infaunal activity, we only sieved some cores for infauna later in the experiment when evidence of infauna was apparent on the sediment surface (Fig. 7e).

Over the first 2 weeks after resuspension, there was little visible infaunal presence (e.g., tubes, fecal mounds, burrows viewed from the side of the core) and infauna likely did not substantially impact surface and subsurface sediment properties. During this period, erosion decreased, consistent with surface reconsolidation (Figs. 5, 6). Previous work in undisturbed natural muds has shown that small-scale (< 1 mm) surface layering can be detected as changing erosion with increasing shear stress (Amos et al. 1992; Thomsen and Gust 2000). Small-scale surface layering as well as different reconsolidation rates between layers is consistent with differences in turbidity and eroded mass between shear stress levels and over time in this study, especially before infauna appeared to influence sediment properties.

Over the first week after resuspension, elevated turbidity and eroded mass at 0.1 and 0.2 Pa coincided with erosion of low-density surface aggregates, consistent with erosion of muds at low shear stresses shown in other studies (Figs. 5b,c, 6b,c) (Amos et al. 1992; Thomsen and Gust 2000; Law and Hill 2019). Higher and more slowly declining SSC and decreasing eroded mass at 0.3 Pa may have showed the beginning of erosion of the more consolidated bed beneath the surface "fluff" layer that took longer to restrengthen (Thomsen and Gust 2000) (Figs. 5d, 6d). The highest shear stresses, 0.45 and 0.6 Pa, caused scouring, indicating mass failure of consolidated layers (Amos et al. 1992) (Fig. 7b; Supporting Information Video S1). Based on rapid stabilization of eroded mass at 0.45 and 0.6 Pa over the first day and turbidity at 0.45 Pa over the first week, these high shear stresses likely exceeded the critical shear stress of the near-surface consolidated layer regardless of the stage of reconsolidation (Figs. 5e, 6e,f).

Changes to cohesion occurring after 2 weeks following resuspension were likely due in large part to infaunal activity. Erosion at all shear stresses had declined from 1–2 d to 2 weeks after resuspension, suggesting a transition from loose, low-density aggregates and weaker underlying layers to a more cohesive surface (Figs. 5, 6). Between 2 and 4 weeks, however, eroded mass at higher shear stresses (0.3–0.6 Pa) appeared to increase even as turbidity remained low (Figs. 5, 6a,d–f). This mass increase occurred as eroded material changed from small particles to larger but discrete particles mostly made up of annelid fecal pellets from scattered fecal mounds (Fig. 7; Supporting Information Video S1). Mucus adhesion likely reduced mound erosion, and individual pellets were likely denser than nonfecal-pellet aggregates eroded at low shear stress at earlier time points and therefore were not eroded as much at 0.1 and 0.2 Pa (Nowell et al. 1981; Drake et al. 2002; Friedrichs et al. 2008) (Figs. 5b,c, 6b,c). In addition, these pellets stayed more intact as they were entrained compared to eroded material from the consolidated layer, resulting in increased eroded mass but less murky water (Figs. 5d–f, 6d–f, 7c; Supporting Information Video S1). This is consistent with low erodibility and SSC coinciding with heavily pelletized estuarine sediment in the York River (Friedrichs et al. 2008; Dickhudt et al. 2009).

The spionid annelids present in this study also constructed tubes at the surface which in high enough densities and with mucus adhesion can stabilize the sediment surface (Eckman et al. 1981; Thrush et al. 1996). High tube densities were observed in Day 30 C, and stabilization was reflected by turbidity no longer exceeding the threshold while the accumulating fecal pellets contributed substantially to the late eroded mass increase (Figs. 5c,e,f, 6d–f, 7e; Supporting Information Video S1). The recovery of the infaunal community, even one consisting mainly of small-bodied and early-colonizing animals, dramatically altered erosion and thus sediment transport dynamics. Transport distance would likely be lower with infauna present due to both lower suspension at low shear stress and dense pellets rather than fine grains comprising much of the suspended load at high shear stress.

Delayed infaunal effects on post-disturbance subsurface compaction and cohesion

Besides altering erosion, delayed infaunal recovery likely affected temporal changes to subsurface sediment properties. Creation of water-filled burrows can increase porosity and reduce sound speed (Rhoads and Boyer 1982; Jones and Jago 1993; Dorgan et al. 2020). This is consistent with the decrease in sediment compaction between 2 and 4 weeks post disturbance after compaction had previously been increasing

(Figure legend continued from previous page.)

Fig. 5. Turbidity as a measure of surface cohesion. (a) Time fraction where turbidity exceeded transmissometer threshold of 0.07 kg m^3 at each shear stress level (stacked bars) at each time point ($n = 3–4$). Bars are st. dev. Maximum suspended sediment concentration (SSC; kg m^3) vs. time post dis-turbance at 0.1 Pa (b) and 0.3 Pa shear stress levels (d) and time fraction above turbidity threshold vs. time post disturbance at 0.2 Pa (c), 0.45 Pa (e) and 0.6 Pa shear stress levels (f). Solid and dashed lines indicate asymptotic fit and 95% CI, respectively, of the form $C_s(t) = a \; (a \; b) * e^{c*t}$, where C_s is SSC, t is day post disturbance, a is 0.0105 (b) and 0.0158 (d), b is 0.0508 (b) and 0.0517 (d), and c is 0.664 (b) and 0.119 (d). For 0.2, 0.45, and 0.6 pa, asymptotic fits are of the form $P(t) = a \; (a \; b) * e^{c*t}$, where P is time fraction above threshold, t is day post disturbance, a is 0 (c,e,f), b is 0.017 (c), 0.164 (e) and 0.165 (f), and c is 0.320 (c), 0.438 (e) and 0.081 (f). Vertical dotted line indicates time at which SSC or time fraction stabilizes close to the asymptote. Time fraction above threshold at 0.6 Pa (f) stabilized by 36.9 d post disturbance. "" symbols indicate the excluded core, Day 30 C, which had murky overlying water before erosion, much higher sand content, and no animal tubes or fecal mounds on the surface. Note that y-axis scale for 0.2 Pa is almost an order of magnitude smaller than that of 0.45 and 0.6 Pa.

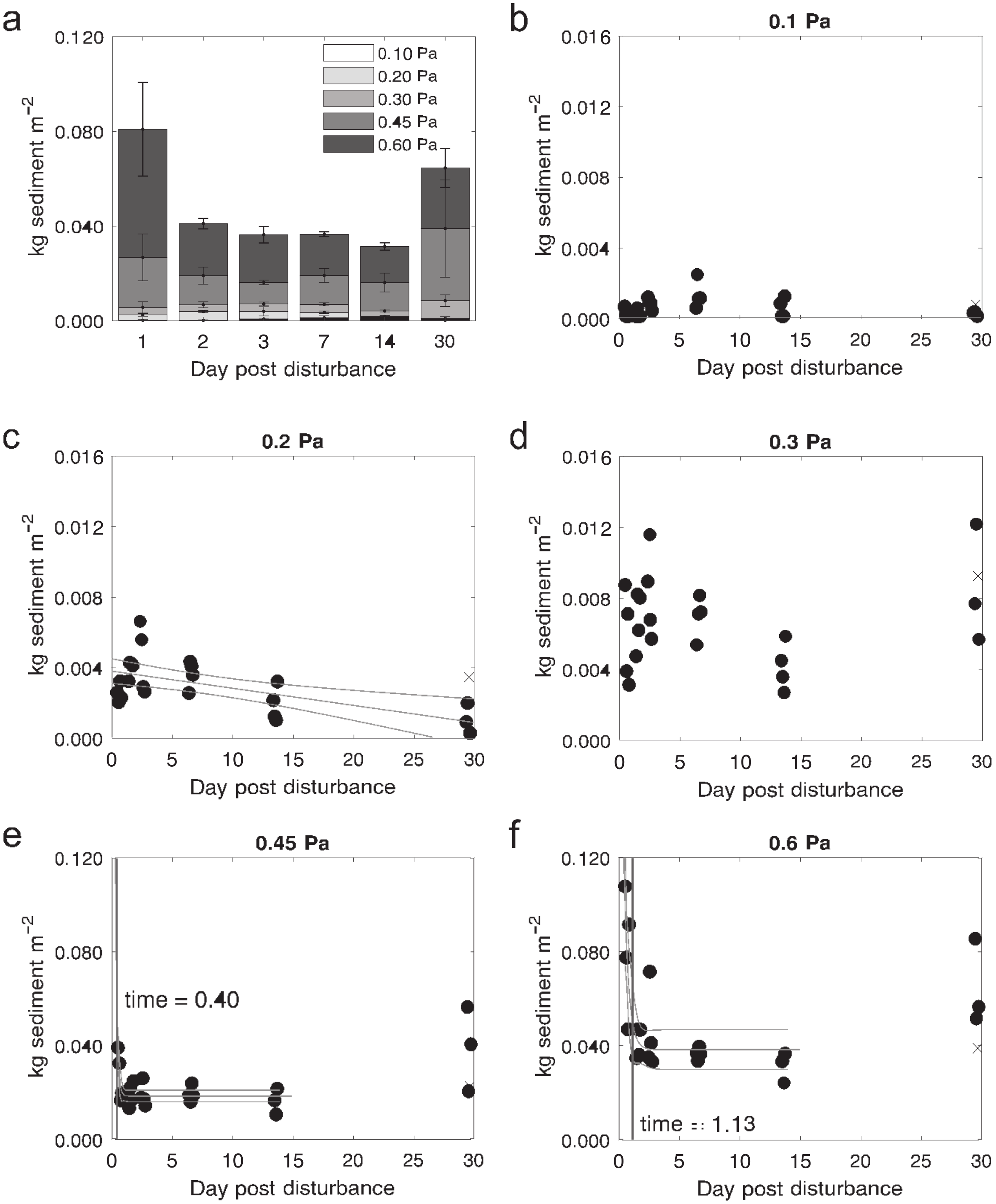

Fig. 6. Cumulative eroded mass at each shear stress level (stacked bars) at each time point (n = 3–4) (a). Bars are 1 standard deviation. Eroded mass vs. time post disturbance at 0.1 Pa (b), 0.2 Pa (c), 0.3 Pa (d), 0.45 Pa (e) and 0.6 Pa shear stress levels (f). Solid and dashed lines indicate fits and 95% CI, respectively, for linear (c) and asymptotic (e,f) fits of the form E(t) = a + b * t, where E is eroded mass (kg m^2), t is day post disturbance, a is 0.0038 and b is 9.73 10^5 (c) and E(t) = a (a b) * e^{c*t}, where a is 0.0182 (e) and 0.0382 (f), b is 0.786 (e) and 0.226 (f), and c is 7.49 (e) and 2.65 (f). Vertical dotted line indicates time at which eroded mass stabilizes close to the asymptote for day 1 to 14. “” symbols indicate the excluded core, Day 30 C, which had murky overlying water before erosion, much higher sand content, and no animal tubes or fecal mounds on the surface. Note differ-ent y-axes between b–d and e–f.

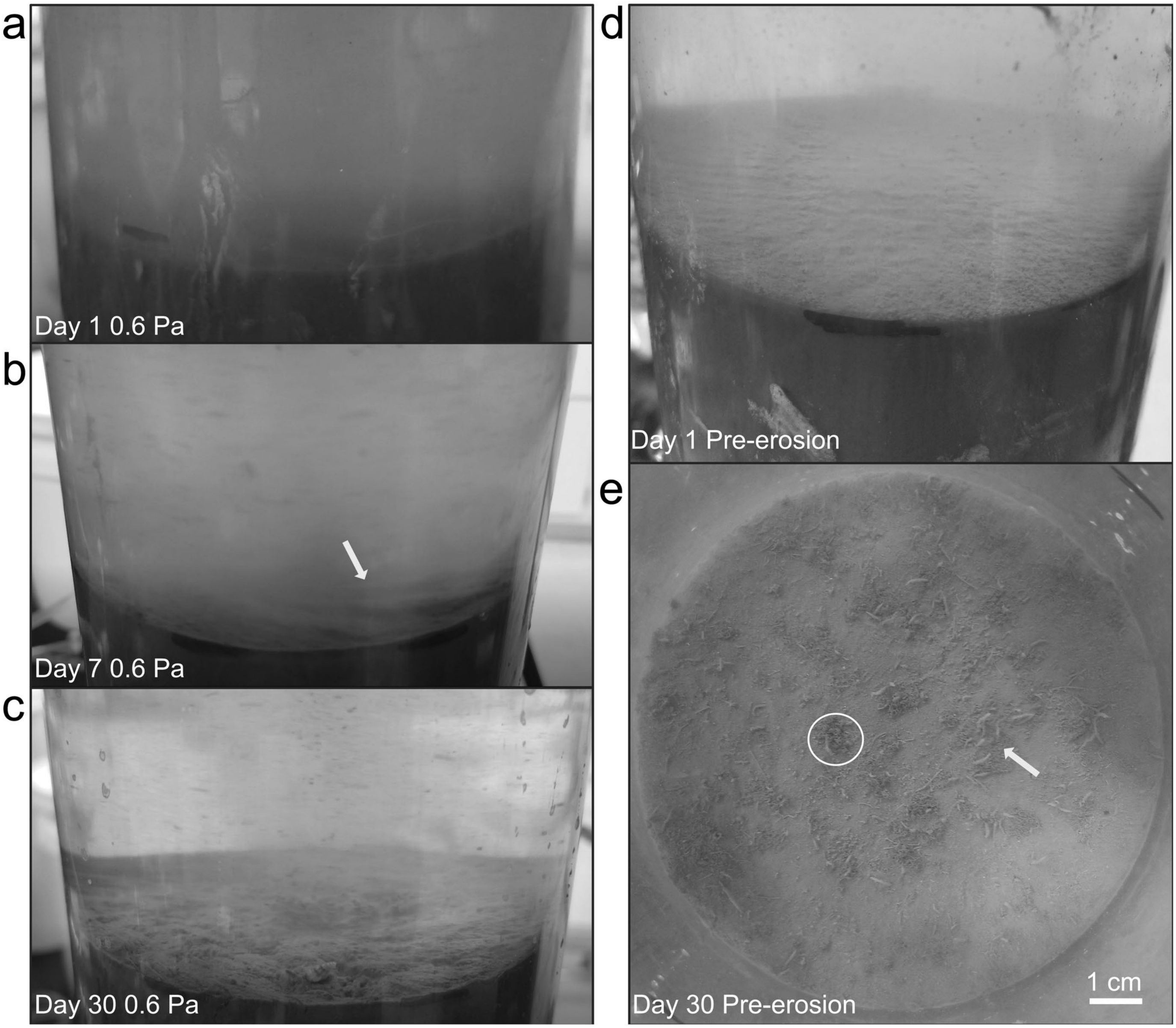

Fig. 7. Core photographs showing erosion occurring at the beginning of the 0.6 Pa level on Days 1 (a), 7 (b), and 30 (c) and core surfaces before ero-sion on Day 1 (d) and Day 30 (e). Arrows indicate scoured furrow (b) and worm tube cluster (e). Circle indicates fecal pellet mound (darker than sur-rounding sediment) (e). Cores are 10 cm in diameter.

(Figs. 3, 4a,b,d). In addition, tube and mound creation increased surface topography that may have obscured small compaction changes from being captured by coarse sediment surface height measurement (Figs. 2, 7e).

Subsurface cohesion, interpreted as force required to break sediment under tension, was negatively related to sediment porosity (Fig. 8b,d,f). Johnson et al. (2012) and Barry et al. (2013) also found that fracture toughness, which is calculated from maximum tensile force, increased with decreasing porosity in cohesive tidal flat sediments. However, within the disturbed layer, cohesion continued to increase after compaction reached an apparent minimum after 2 weeks. Subsurface cohesion at 3 cm did not stabilize until almost 3 weeks post disturbance, and cohesion at 4 cm continued to increase over time (Fig. 8a,c), suggesting that the cohesive matrix of subsurface sediment continued to develop even as burrowing activity increased porosity. Although burrow excavation creates large water-filled voids, it also compacts the sediment at the burrow walls (Dorgan 2015). In addition, burrowing annelids produce mucus and irrigate sediments, binding sediment grains and

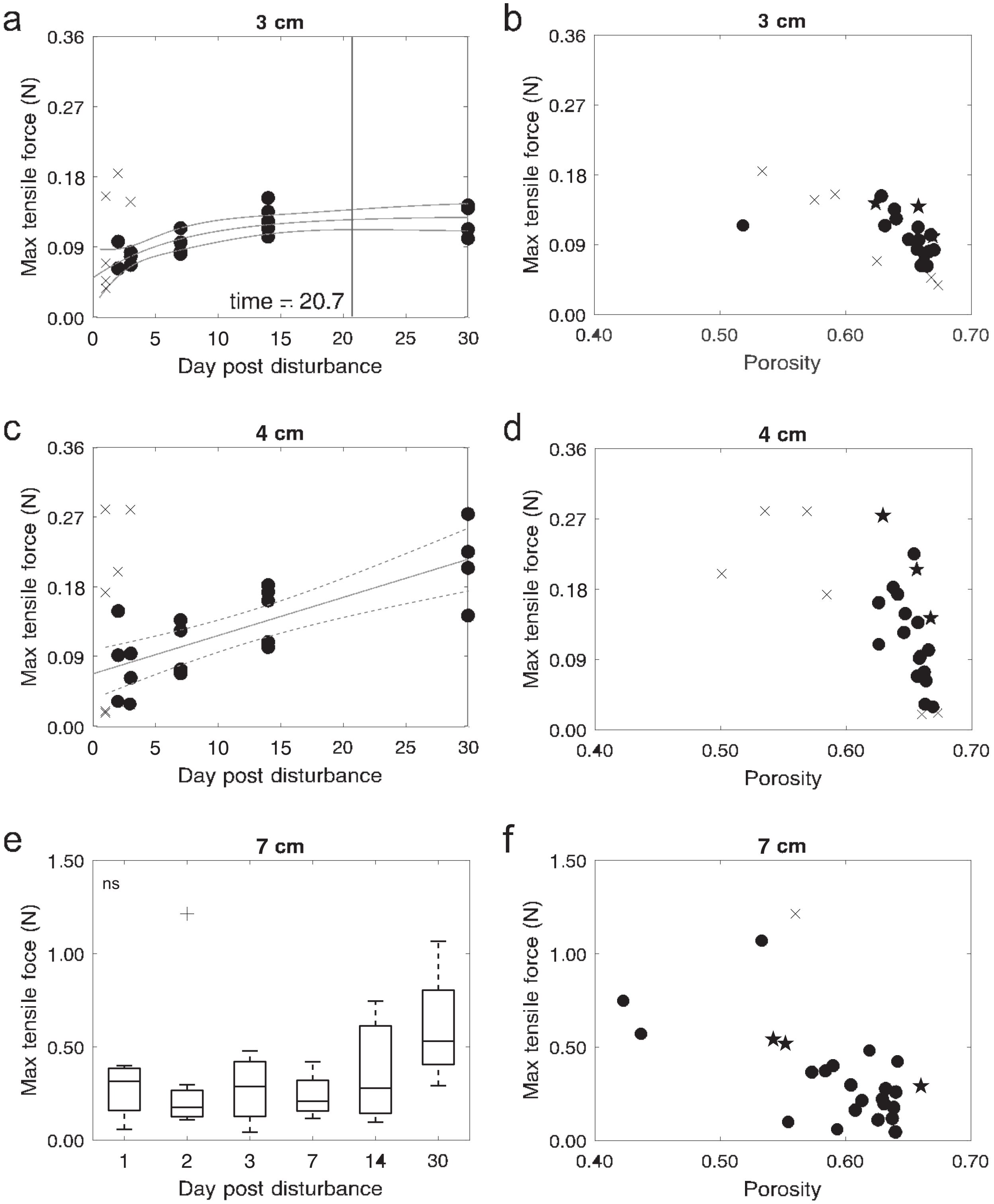

Fig. 8. Maximum tensile force vs. time post disturbance at 3 cm (a), 4 cm (c) and 7 cm depths (e) and maximum tensile force vs. porosity at 3 cm (b), 4 cm (d), and 7 cm (f). Solid and dashed lines indicate fits and 95% CI, respectively, for asymptotic (a) and linear (c) fits of the form F(t) = a (a b) * e^{c*t}, where F is tensile force (N), t is day post disturbance, a is 0.129, b is 0.051, and c is 0.144 (a) and F(t) = a + b * t, where a is 0.068 and b is 0.005 (c). Vertical dotted line indicates time at which tensile force stabilizes close to the asymptote (a). Star symbols indicate Day 30 data (b,d,f). “” symbols indicate excluded data (a–d,f). Force data at 7 cm are grouped by time point (n = 3–5; e). “+” symbol indicates Day 2 D. “ns” indicates no significant differences among timepoints. Note different y-axis scale at 7 cm (e,f).

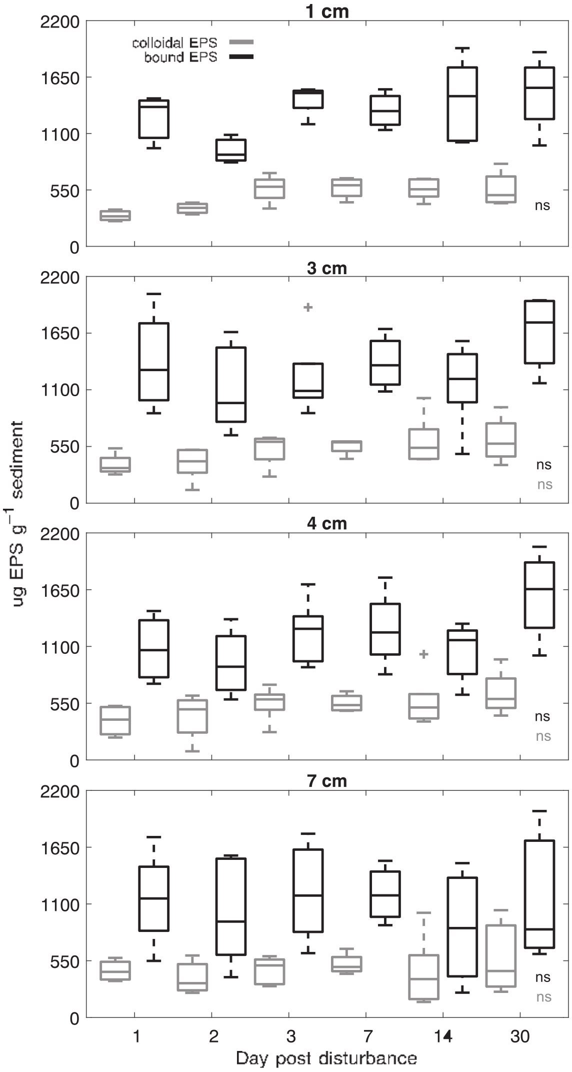

Fig. 9. Colloidal (gray) and sediment-bound (black) EPS carbohydrate concentration at each time point at 1, 3, 4, and 7 cm depths (n = 3–5). Boxplots are the same configuration as in Fig. 3. "ns" indicates no significant differences among timepoints.

stimulating microbial growth and potential EPS production (Meadows et al. 1990; Passarelli et al. 2012).

EPS concentration is not correlated with post-disturbance cohesion

Studies suggest microbial EPS plays an important role in surface and bulk sediment stability (Thomsen and Gust 2000; Malarkey et al. 2015), and we expected that, even with infauna, sediment cohesion would be proportional to EPS concentration. In this study, however, EPS exhibited no post-disturbance temporal changes, rather changes to subsurface cohesion were more closely related to sediment compaction (Figs. 8b,d,f, 9; Supporting Information Fig. S2). The lack of correlation between subsurface cohesion and EPS concentration points to the importance of the structure as well as the amount of EPS. Physical disturbance would not necessarily remove EPS but could disrupt the EPS-sediment matrix or links between sediment grain-EPS aggregates. Thus, while the amount of EPS did not change significantly over time post disturbance, the bonds between EPS-sediment aggregates that form the cohesive sediment-organic matrix likely continued to increase over time. This re-bonding likely also depends on microbial activity producing the EPS matrix and "gluing" it to sediment grains (Lubarsky et al. 2010; Chen et al. 2017).

Bacteria and diatoms produce EPS biofilms consisting of polymers cross-linked by cations (Decho 2000, Wloka et al., 2004, de Brouwer et al. 2005). Studies have shown that biofilm development and EPS production by bacteria and mixed bacteria-diatom cultures increase surface cohesion over 25–35 d (Gerbersdorf et al. 2009; Lubarsky et al. 2010). Furthermore, Chen et al. (2017) found that bacterial EPS production reduced erosion in the top 5 mm of sediment over time until it stabilized 16 d after inoculation. These timescales of increasing microbial stabilization are consistent with the stabilization or increases in several metrics of surface and subsurface cohesion in this study (Figs. 5d,f, 6b,c, 8a,c). Thus, a post-disturbance lag of microbial activity restructuring the EPS matrix may partially explain cohesion changes without EPS concentration changes. Furthermore, while sediment organic matter is speculated to influence subsurface cohesion (Johnson et al. 2012), it is not presently clear whether microbial EPS biofilm stabilization of surface sediment translates to the redevelopment of the gel-like cohesive structure of subsurface muddy sediment, especially with the added force of compaction from overlying sediment that likely increases cohesion (Fig. 8e). Understanding bulk sediment-organic matrix redevelopment is especially important regarding subsequent mass movement of recently disturbed sediment.

Conclusions

Compaction and cohesion of muddy sediments following physical disturbance occurred more quickly at the sediment surface than in subsurface sediments, although temporal patterns also reflected biological effects, particularly a delayed but substantial impact of small infauna. These results suggest that infauna surviving physical disturbance likely play an important role in re-strengthening muddy sediment following a disturbance. Infaunal recovery and burrowing activity several weeks after disturbance likely led to decreased sediment density, increased surface and subsurface cohesion and accumulation of tubes and fecal pellets. After adult infauna rebuilt burrows and tubes or juveniles matured into adults, their burrowing activity may have facilitated the reconstruction of the sediment-organic matrix by burrow compaction, mucus production, and stimulation of microbial activity. That small "pioneering" infauna species substantially altered disturbed sediment reconsolidation demonstrates the importance of examining rates of biological change in addition to physical change, even in heavily disturbed sediments such as anthropogenic deposits from sediment diversions, dredge spoil placement and dredged channel slopes that may have few infauna and/or slow community recovery. Timescales of natural muddy sediment recovery, including that of their biological communities, are important to understand in order to assess susceptibility of disturbed sediment to further physical disturbance, especially for shallow coastal muds which are important sites of navigation and construction and may face more intense storms as the climate warms.

Data availability statement

The data that support the findings of this study are openly available from the National Science Foundation Biological and Chemical Oceanography Data Management Office under the project CAREER: Mechanisms of bioturbation and ecosystem engineering by benthic infauna at http://lod.bco-dmo.org/id/dataset/875501 (Dorgan and Clemo 2022a), http://lod.bco-dmo.org/id/dataset/875514 (Dorgan and Clemo 2022b), http://lod.bco-dmo.org/id/dataset/875391 (Dorgan and Clemo 2022c), and http://lod.bco-dmo.org/id/dataset/875373 (Dorgan and Clemo 2022d).

References

Albalasmeh, A. A., A. A. Berhe, and T. A. Ghezzehei. 2013. A new method for rapid determination of carbohydrate and total carbon concentrations using UV spectrophotometry. Carbohydr. Polym. 97: 253–261. doi:10.1016/j.carbpol.2013.04.072

Aller, R. C. 2004. Conceptual models of early diagenetic processes: The muddy sea floor as an unsteady, batch reactor. J. Mar. Res. 62: 815–835.

Allison, M. A., T. M. Dellapenna, E. S. Gordon, S. Mitra, and S. T. Petsch. 2010. Impact of Hurricane Katrina (2005) on shelf organic carbon burial and deltaic evolution. Geophys. Res. Lett. 37: 1–5. doi:10.1029/2010GL044547

Amos, C. L., G. R. Daborn, H. A. Christian, A. Atkinson, and A. Robertson. 1992. In situ erosion measurements on fine-grained sediments from the Bay of Fundy. Mar. Geol. 108: 175–196.

Avnimelech, Y., G. Ritvo, L. E. Meijer, and M. Kochba. 2001. Water content, organic carbon and dry bulk density in flooded sediments. Aquacult. Eng. 25: 25–33.

Barry, M., and others. 2013. Sedimentary and geo-mechanical properties of Willapa Bay tidal flats. Continent. Shelf Res. 60: S198–S207. doi:10.1016/j.csr.2012.05.007

Bentley, S. J., T. R. Keen, C. Ann, and W. C. Vaughan. 2002. The origin and preservation of a major hurricane event bed in the northern Gulf of Mexico: Hurricane Camille, 1969. Mar. Geol. 186: 423–446.

Boudreau, B. P. 1998. Mean mixed depth of sediments: The wherefore and the why. Limnol. Oceanogr. 43: 524–526. doi:10.4319/lo.1998.43.3.0524

Brenchley, G. 1981. Disturbance and community structure: An experimental study of bioturbation in marine soft-bottom environments. J. Mar. Res. 39: 767–790.

Buckingham, M. J. 2005. Compressional and shear wave properties of marine sediments: Comparisons between theory and data. J. Acoust. Soc. Am. 117: 137–152.

Chen, X. D., C. K. Zhang, D. M. Paterson, C. E. L. Thompson, I. H. Townend, Z. Gong, Z. Zhou, and Q. Feng. 2017. Hindered erosion: The biological mediation of noncohesive sediment behavior. Water Resour. Res. 53: 4787–4801. doi:10.1002/2016WR020105.Received

de Brouwer, J. F. C., and L. J. Stal. 2001. Short-term dynamics in microphytobenthos distribution and associated extracellular carbohydrates in surface sediments of an intertidal mudflat. Mar. Ecol. Prog. Ser. 218: 33–44.

de Brouwer, J. F. C., K. Wolfstein, G. K. Ruddy, T. E. R. Jones, and L. J. Stal. 2005. Biogenic stabilization of intertidal sediments: The importance of extracellular polymeric substances produced by benthic diatoms. Microb. Ecol. 49: 501–512. doi:10.1007/s00248-004-0020-z

Decho, A. W. 2000. Microbial biofilms in intertidal systems: An overview. Cont. Shelf Res. 20: 1257–1273.

Dickhudt, P. J., C. T. Friedrichs, L. C. Schaffner, and L. P. Sanford. 2009. Spatial and temporal variation in cohesive sediment erodibility in the York River estuary, eastern USA: A biologically influenced equilibrium modified by seasonal deposition. Mar. Geol. 267: 128–140. doi:10.1016/j.margeo.2009.09.009

Dorgan, K. M. 2015. The biomechanics of burrowing and boring. J. Exp. Biol. 218: 176–183. doi:10.1242/jeb.086983

Dorgan, K. M., P. A. Jumars, B. Johnson, B. P. Boudreau, and E. Landis. 2005. Burrow extension by crack propagation. Nature 433: 475.

Dorgan, K. M., W. Ballentine, G. Lockridge, E. Kiskaddon, M. S. Ballard, K. M. Lee, and P. S. Wilson. 2020. Impacts of simulated infaunal activities on acoustic wave propagation in marine sediments. J. Acoust. Soc. Am. 2: 812–823. doi:10.1121/10.0000558

Dorgan, K., Clemo, W. C. 2022a. Acoustic properties of sediments collected from the Northern Gulf of Mexico following laboratory resuspension at the Dauphin Island sea lab. Biological and Chemical Oceanography Data Management Office (BCO-DMO) (Version 1). Version Date 15 June 2022. [dataset]. Available from http://lod.bco-dmo.org/id/dataset/875501

Dorgan, K., Clemo, W. C. 2022b. Elevation of sediments collected from the Northern Gulf of Mexico following laboratory resuspension at the Dauphin Island Sea Lab. Biological and Chemical Oceanography Data Management Office (BCO-DMO). (Version 1) Version Date 2022-06-15 [dataset]. Available from http://lod.bco-dmo.org/id/dataset/875514

Dorgan, K., Clemo, W. C. 2022c. Erodibility of sediments collected from the northern Gulf of Mexico following laboratory resuspension at the Dauphin Island Sea Lab. Biological and Chemical Oceanography Data Management Office (BCO-DMO). (Version 1) Version Date 2022-06-24 [dataset]. Available from http://lod.bco-dmo.org/id/dataset/875391

Dorgan, K., Clemo, W. C. 2022d. Elevation, erodibility, and acoustic properties of sediments collected from the Northern Gulf of Mexico following resuspension at the Dauphin Island Sea Lab in 2020. Biological and Chemical Oceanography Data Management Office (BCO-DMO). (Version 1) Version Date 2022-06-28 [dataset]. Available from http://lod.bco-dmo.org/id/dataset/875373

Drake, D. E., R. Eganhouse, and W. Mcarthur. 2002. Physical and chemical effects of grain aggregates on the Palos Verdes margin, southern California, Cont. Shelf Res. 22: 967–986.

Dubois, M., K. A. Gilles, J. K. Hamilton, P. A. Rebers, and F. Smith. 1956. Colorimetric method for determination of sugars and related substances. Anal. Chem. 28: 350–356. doi:10.1021/ac60111a017

Eagle, R. A. 1973. Benthic studies in the south east of Liverpool Bay. Estuar. Coast. Mar. Sci. 1: 285–299.

Eckman, J. E., A. R. M. Nowell, and P. a Jumars. 1981. Sediment destabilization by animal tubes. J. Mar. Res. 39: 361–374.

Emanuel, K. 2017. Will global warming make hurricane forecasting more difficult? Bull. Am. Meteorol. Soc. 98: 495–502. doi:10.1175/BAMS-D-16-0134.1

Folk, R. L., and W. C. Ward. 1957. Brazos River Bar: A study in the significance of grain size parameters. J. Sediment. Res. 27: 3–26.

Friedrichs, C. T., G. M. Cartwright, and P. J. Dickhudt. 2008. Quantifying benthic exchange of fine sediment via continuous, noninvasive measurements of settling velocity and bed erodibility. Oceanography 21: 168–172.

Gerbersdorf, S. U., R. Bittner, H. Lubarsky, W. Manz, and D. M. Paterson. 2009. Microbial assemblages as ecosystem engineers of sediment stability. J. Soil. Sediment. 9: 640–652. doi:10.1007/s11368-009-0142-5

Green Eyes LLC. 2015. U-GEMS manual version 3.0. 0-44.

Gust, G., and V. Muller. 1997. Interfacial hydrodynamics and entrainment functions of currently used erosion devices, p. 149–174. In N. Burt [ed.], Cohesive Sediments: 4th Nearshore and Estuarine Cohesive Sediment Transport Conference, INTERCOH ‘94, 11–15 July 1994. Wiley.

Jackson, D. R., and M. D. Richardson. 2007. High-frequency seafloor acoustics. Springer.

Johnson, B. D., B. P. Boudreau, B. S. Gardiner, and R. Maass. 2002. Mechanical response of sediments to bubble growth. Mar. Geol. 187: 347–363.

Johnson, B. D., M. A. Barry, B. P. Boudreau, P. A. Jumars, and K. M. Dorgan. 2012. In situ tensile fracture toughness of surficial cohesive marine sediments. Geo-Marine Lett. 32: 39–48. doi:10.1007/s00367-011-0243-1

Jones, S. E., and C. E. Jago. 1993. In situ assessment of modification of sediment properties by burrowing invertebrates. Mar. Biol. 115: 133–142.

Jumars, P. A., K. M. Dorgan, and S. M. Lindsay. 2015. Diet of worms emended: An update of polychaete feeding guilds. Ann. Rev. Mar. Sci. 7: 497–520. doi:10.1146/annurev-marine-010814-020007

Knutson, T., S. J. Camargo, J. C. L. Chan, K. Emanuel, C. Ho, J. Kossin, M. Mohapatra, and M. Satoh. 2020. Tropical cyclones and climate change assessment. Bull. Am. Meteorol. Soc. 101: 303–322.

Law, B. A., and P. S. Hill. 2019. Spatial and temporal variation in cumulative mass eroded and organic matter percentage in surface sediments near areas of active salmon aquaculture. Aquacult. Environ. Interact. 11: 305–320.

Lo, E. L., S. J. Bentley, and K. Xu. 2014. Experimental study of cohesive sediment consolidation and resuspension identifies approaches for coastal restoration: Lake Lery, Louisiana. Geo-Mar. Lett 34: 499–509. doi:10.1007/s00367-014-0381-3

Lubarsky, H. V., C. Hubas, M. Chocholek, F. Larson, W. Manz, D. M. Paterson, and S. U. Gerbersdorf. 2010. The stabilisation potential of individual and mixed assemblages of natural bacteria and microalgae. PLoS One 5: 1–12. doi: 10.1371/journal.pone.0013794

Lundkvist, M., M. Grue, P. L. Friend, and M. R. Flindt. 2007. The relative contributions of physical and microbiological factors to cohesive sediment stability. Cont. Shelf Res. 27: 1143–1152. doi:10.1016/j.csr.2006.01.021

Malarkey, J., and others. 2015. The pervasive role of biological cohesion in bedform development. Nat. Commun. 6: 1–6. doi:10.1038/ncomms7257

McAnally, W., C. Friedrichs, D. Hamilton, E. Hayer, P. Shrestha, H. Rodriguez, and S. A, and A. Teeter. 2007. Management of fluid mud in estuaries, bays, and lakes. I: Present state of understanding on character and behavior. J. Hydraul. Eng. 133: 9–22. doi:10.1061/(ASCE)0733-9429(2007)133

McKee, B. A., R. C. Aller, M. A. Allison, T. S. Bianchi, and G. C. Kineke. 2004. Transport and transformation of dissolved and particulate materials on continental margins influenced by major rivers: Benthic boundary layer and seabed processes. Cont. Shelf Res. 24: 899–926. doi:10.1016/j.csr.2004.02.009

Meadows, P. S., J. Tait, and S. A. Hussain. 1990. Effects of estuarine infauna on sediment stability and particle sedimentation. Hydrobiologia 190: 263–266.

Montserrat, F., C. Van Colen, S. Degraer, T. Ysebaert, and P. M. J. Herman. 2008. Benthic community-mediated sediment dynamics. Mar. Ecol. Prog. Ser. 372: 43–59. doi:10.3354/meps07769

Morton, R. A. 1988. Near shore responses to great storms. Geol. Soc. Am.: 7–22.

Nowell, A. R. M., P. A. Jumars, and J. E. Eckman. 1981. Effects of biological activity on the entrainment of marine sediments. Mar. Geol. 42: 133–153. doi:10.1016/0025-3227(81)90161-4

Passarelli, C., F. Olivier, D. M. Paterson, and C. Hubas. 2012. Impacts of biogenic structures on benthic assemblages:

Microbes, meiofauna, macrofauna and related ecosystem functions. Mar. Ecol. Prog. Ser. 465: 85–99. doi:10.3354/meps09915

Pearson, T., and R. Rosenberg. 1978. Macrobenthic succession in relation to organic enrichment and polution of the marine environment. Oceanogr. Mar. Biol. Anu. Rev. 16: 229–311.

Queiros, A. M., and others. 2013. A bioturbation classification of European marine infaunal invertebrates. Ecol. Evol. 3: 3958–3985. doi:10.1002/ece3.769

Rabaut, M., K. Guilini, G. Van Hoey, M. Vincx, and S. Degraer. 2007. A bio-engineered soft-bottom environment: The impact of Lanice conchilega on the benthic species-specific densities and community structure. Estuar. Coast. Shelf Sci. 75: 525–536. doi:10.1016/j.ecss.2007.05.041

Rhoads, D. C., and L. F. Boyer. 1982. The effects of marine benthos on physical properties of sediments, p. 3–52. In P. L. McCall and M. J. S. Tevesz [eds.], Animal-sediment relations. Springer.

Ross, M. A., and A. J. Mehta. 1989. On the mechanics of lutoclines and fluid mud. J. Coast. Res.: 51–61.

Soissons, L. M., T. Gomes, J. Bastiaan, J. Van Dalen, T. Ysebaert, P. M. J. Herman, F. Cozzoli, and T. J. Bouma. 2019. Sandification vs. muddification of tidal flats by benthic organisms: A flume study. Estuar. Coast. Shelf Sci. 228: 1–8.

Sokal, R. R., and F. J. Rohlf. 2012. Biometry, 4th ed. W. H. Freeman and Company.

Thomsen, L., and G. Gust. 2000. Sediment erosion thresholds and characteristics of resuspended aggregates on the western European continental margin. Deep. Res. Part I Oceanogr. Res. Pap. 47: 1881–1897. doi:10.1016/S0967-0637(00)00003-0

Thrush, A. S. F., R. B. Whitlatch, R. D. Pridmore, J. E. Hewitt, V. J. Cummings, and M. R. Wilkinson. 1996. Scale-dependent recolonization: The role of sediment stability in a dynamic sandflat habitat. Ecology 77: 2472–2487.

Thrush, S. F., J. E. Hewitt, A. Norkko, P. E. Nicholls, G. A. Funnell, and J. I. Ellis. 2003. Habitat change in estuaries: Predicting broad-scale responses of intertidal macrofauna to sediment mud content. Mar. Ecol. Prog. Ser. 263: 101–112.

Tolhurst, T. J., M. Consalvey, and D. M. Paterson. 2008. Changes in cohesive sediment properties associated with the growth of a diatom biofilm. Hydrobiologia 596: 225–239. doi:10.1007/s10750-007-9099-9

Volkenborn, N., S. Hedtkamp, J. van Beusekom, and K. Reise. 2007. Effects of bioturbation and bioirrigation by lugworms (Arenicola marina) on physical and chemical sediment properties and implications for intertidal habitat succession. Estuar. Coast. Shelf Sci. 74: 331–343. doi:10.1016/j.ecss.2007.05.001

Watling, L. 1988. Small-scale features of marine sediments and their importance to the study of deposit-feeding. Mar. Ecol. Prog. Ser. 47: 135–144.

Wheatcroft, R. A., P. L. Wiberg, C. R. Alexander, S. J. Bentley, D. E. Drake, C. K. Harris, and A. S. Ogston. 2007. Post-depositional alteration and preservation of sedimentary strata. Cont. Margin Sediment 101–155. doi:10.1002/9781444304398.ch3

Wiberg, P. L., B. A. Law, R. A. Wheatcroft, T. G. Milligan, and P. S. Hill. 2013. Seasonal variations in erodibility and sediment transport potential in a mesotidal channel-flat complex, Willapa Bay, WA. Cont. Shelf Res. 60: S185–S197. doi:10.1016/j.csr.2012.07.021

Widdows, J., M. D. Brinsley, P. N. Salkeld, and C. H. Lucas. 2000. Influence of biota on spatial and temporal variation in sediment erodability and material flux on a tidal flat (Westerschelde, The Netherlands). Mar. Ecol. Prog. Ser. 194: 23–37.

Widdows, J., and others. 2004. Role of physical and biological processes in sediment dynamics of a tidal flat in Westerschelde Estuary, SW Netherlands. Mar. Ecol. Prog. Ser. 274: 41–56.

Wloka, M., H. Rehage, H.C. Flemming, and J. Wingender. 2004. Rheological properties of viscoelasticbiofilm extracellular polymeric substances and comparison to the behavior ofcalcium alginate gels. Colloid Polym. Sci. 282: 1067–1076. doi:10.1007/s00396-003-1033-8

Wynberg, R. P., and G. M. Branch. 1994. Disturbance associated with bait-collection for sandprawns (Callianassa kraussi) and mudprawns (Upogebia africana): Long-term effects on the biota of intertidal sandflats. J. Mar. Res. 52: 523–558.

Yallop, M. L., B. de Winder, D. M. Paterson, and L. J. Stal. 1994. Comparative structure, primary production and biogenic stabilization of cohesive and non-cohesive marine sediments inhabited by microphytobenthos. Estuar. Coast. Shelf Sci. 39: 565–582.

Acknowledgments

This project was funded by the ONR Young Investigator Program Award #N00014-17-1-2625 and National Science Foundation CAREER grant OCE #1844910. The authors thank G. Lockridge for help in erosion chamber construction, fracture probe construction and operation, and core collection, D. Wallace for Mastersizer use, K. Hoadley for plate reader use and EPS analysis advice, J. Krause for vacuum filter use and EPS analy-sis advice, S. Wang, A. Robertson, and L. Linn for EPS analysis advice, Dau-phin Island Sea Lab captains for piloting the RV Alabama Discovery and core collection, and C. Cox, W. Ballentine, K. Baltzer, M. Frey, L. Byrd, S. Sirk Morato, and K. Gadeken for core collection, experimental measure-ments, and sample processing.

Conflict of Interest

None declared.

Submitted 11 March 2022
Revised 06 June 2022
Accepted 11 August 2022

Associate editor: Josef Daniel Ackerman